The 2009 IEEE/RSJ International Conference on
Intelligent Robots and Systems
October 11-15, 2009 St. Louis, USA

Design of a Novel 3 Degree of Freedom Robotic Joint

Mark L. Guckert and Michael D. Naish, *Member, IEEE*

***Abstract*— Spherical joints have evolved into a critical component of many robotic systems, often used to provide dexterity at the wrist of a manipulator. In this work, a novel 3 degree of freedom spherical joint is proposed, actuated by tendons that run along the surface of the sphere. The joint is mechanically simple and avoids mechanical singularities. The kinematics and mechanics of the joint are modeled and used to develop both open and closed loop control systems. Simulated and experimental assessment of the joint performance demonstrates that it can be successfully controlled in 3 degrees of freedom. It is expected that the joint will be a useful option in the development of emerging robotic applications, particularly those requiring miniaturization.**

***Index Terms*— mechanism design, tendon-driven, spherical joint, visual servoing**

I. INTRODUCTION

Spherical joints have become an integral component in robotic applications, commonly comprising both the wrist and shoulder of robotic manipulators. As a result, three degree of freedom (DOF) joints have been studied extensively, with a great deal of work being devoted to the development of transmission systems that route power to and through them. Methods to avoid the creation of the singularities that occur in Euler joints have also been developed. Most of these systems, however effective on the macro scale, do not lend themselves well to miniaturization due to the mechanical complexity inherent in gear trains and similar systems. Aside from being difficult to produce on a small scale, these systems require such a large portion of a device's volume that, when space is limited, the strength of the device may be significantly compromised.

The work presented herein introduces a tendon-driven 3 DOF spherical joint in which the tendons run along the surface of the sphere, as shown in Fig. 1. This approach avoids the Euler singularities inherent to orthogonal rotary joints and maximizes the load bearing structure of the joint through the use of a relatively small tendon transmission system. While previous 3 DOF tendon actuated spherical joints have been devised, such as [1]–[3], the tendons in these systems have all passed through free space, originating and inserting on some sort of frame fixed to either side of the joint. The tendons are assumed to always run along a straight path that requires an uninterrupted volume around the joint. The required free space increases the effective size of the joint as it cannot move through any orientation where the tendons might collide with another object, each other, or with the joint itself. By developing a design where the tendons are assumed to run along the surface of the joint, the available space can be used more effectively. The advantages of this approach for the miniaturization of manipulators is readily obvious. However, for it to be of value in a robotics application position control of the joint must be predictable and accurate.

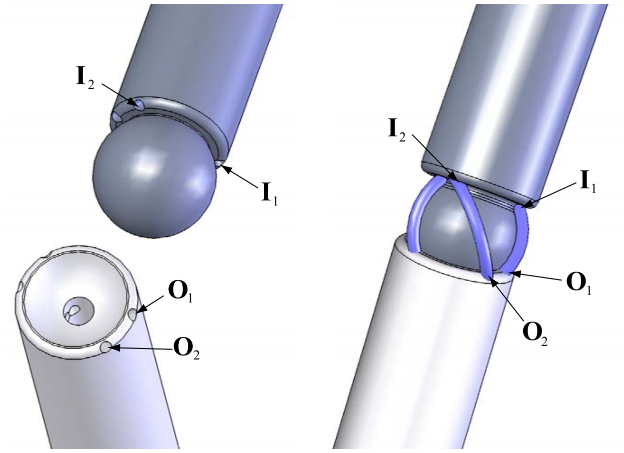

Fig. 1. Solid model of joint ball, socket, and assembly with tendons. Note that only two of four origin-insertion pairs are labeled.

A 2 DOF form of the joint proposed in this work has been successfully explored in [4]. Therein, by choosing an appropriate tendon configuration, the spherical joint was limited to acting in 2 degrees of freedom and could be driven using as few as three tendons. However, to exploit all three mechanical DOF available in the spherical joint, at least 4 tendons must be used to drive it. Herein, the design and control of a 3 DOF spherical joint using 4 tendons that lie on the surface of the sphere is presented.

II. METHOD

A. Inverse Kinematics

The joint structure comprises a redundant parallel mechanism and therefore no closed-form analytical solution to the forward kinematics will exist for most cases [5]. The inherent redundancy requires that the motion of the actuators be coordinated to control the orientation of the distal end of the joint. To achieve this motion, the following relationship

---

Manuscript received March 1, 2009. This research was supported by the Natural Sciences and Engineering Research Council (NSERC) of Canada under grants 312383-05 and 1345-07.

M.L. Guckert is with Canadian Surgical Technologies and Advanced Robotics (CSTAR), 339 Windermere Road, London, ON, Canada and with the Department of Mechanical and Materials Engineering, University of Western Ontario (UWO), London, ON, Canada (email: mguckert@uwo.ca).

M.D. Naish is with CSTAR, the Department of Mechanical and Materials Engineering, and the Department of Electrical and Computer Engineering, UWO, (phone: 519-661-2111 ext. 88294, email: naish@eng.uwo.ca).

between joint and tendon position can be used:

$$L_n = r \arccos\left(\frac{\mathbf{R}\,\mathbf{I}_n}{r} \cdot \frac{\mathbf{O}_n}{r}\right), \tag{1}$$

$$h_n = Li_n - L_n, \tag{2}$$

the derivation of which is described in Appendix I. In these equations, using the convention for tendon driven manipulators presented in [6], h_n is defined as the proximal motion of nth tendon actuator away from the joint. For each tendon, an origin $\mathbf{O}_n$ and insertion point $\mathbf{I}_n$ are defined in Cartesian coordinates on the sphere, relative to the stationary (proximal) and moving (distal) frames respectively. The locations of these points, $\mathbf{O}_n$ and $\mathbf{I}_n$, as they may be used in a potential joint design are shown in Fig. 1, and in a kinematic representation of the joint in Fig. 2. The origins of both frames are defined to be at the center of the joint's sphere of radius r. A rotation matrix $\mathbf{R}$ is defined that represents the 3 DOF rotation of the moving frame relative to the stationary one. With this information, the length of each tendon running along the sphere surface, L_n, can be found. This can then be related to h_n as in (2), where Li_n is the length of the nth tendon prior to joint motion. Note that prior to joint motion, h_n is zero.

Fig. 2 illustrates the underlying kinematics of the joint by substituting curved prismatic joints for the tendons. The curve of the prismatic joints is a circular path concentric to the central spherical joint linking the mobile platform and the base of the manipulator. This fixes all of the origin and insertion points at an equal distance (equivalent to the radius of the ball in the actual design) from the central spherical joint. The legs of the base and moving platform act radially to the ball joint and prismatic joint curves.

From this illustration it can also be seen that the extension of the prismatic actuator (cable length) will be an arc which subtends the angle between the two legs supporting the actuator, as described by (1).

B. Joint Mechanics

From Fig. 2 it may be observed that the two legs attached to each actuator define a plane in which the actuator will lie, and exert forces on the legs. Any torque exerted by an actuator on the central ball joint will therefore be perpendicular to this plane. Thus, torque applied by each tendon on the joint, relative to the fixed frame, can be expressed as:

$$\boldsymbol{\tau}_n = t_n \quad (\mathbf{R}\,\mathbf{I}_n \times \mathbf{O}_n)/r, \tag{3}$$

where t_n is the tension in the tendon and $\boldsymbol{\tau}_n$ is the vector of torques generated around the fixed frame by tendon n. The derivation of this equation is described in Appendix II.

Furthermore, assuming inelastic tendon behavior, a Jacobian matrix $\mathbf{P}(\boldsymbol{\theta})$ that relates the joint torques to tendon tensions and the rates of change in h_n to the angular velocities of the joint can be defined as follows [6]:

$$\mathbf{P}(\boldsymbol{\theta}) = \frac{\partial \mathbf{h}}{\partial \boldsymbol{\theta}}, \tag{4}$$

$$\dot{\mathbf{h}} = \mathbf{P}^T(\boldsymbol{\theta})\ \dot{\boldsymbol{\theta}}, \tag{5}$$

$$\boldsymbol{\tau} = \mathbf{P}(\boldsymbol{\theta})\ \mathbf{t}, \tag{6}$$

where $\mathbf{h}$ is a vector containing the h_n values for all of the individual tendons and $\boldsymbol{\tau}$ is a vector representing the sum of all torque vectors $\boldsymbol{\tau}_n$ generated by the tendons. Both of these features can be exploited for control of the manipulator in path planning, compensation for tendon elasticity, and in the estimation of external forces applied to the end effector.

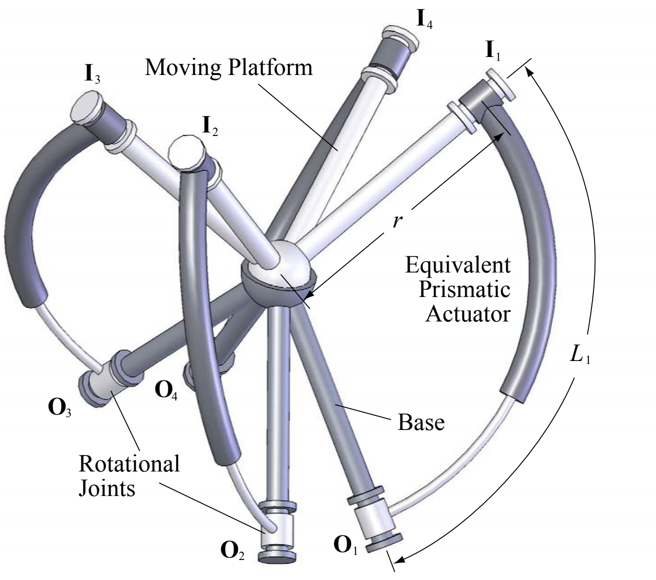

Fig. 2. Kinematic diagram of the idealized joint, with curved prismatic joints illustrating tendon paths.

An important constraint on the design of the joint results from (3). If the tendon origin, insertion and the sphere center become collinear (i.e., $\boldsymbol{\tau}_n$ becomes a zero vector), the path between the origin and the insertion will be the same length, no matter how it runs across the sphere. This results in a singularity in the tendon space, where the direction of the torque applied by the tendon is unknown. To avoid encountering such singularities, the tendon origin and insertion points should be selected such that they will not align with the sphere center at any orientation in the desired workspace.

C. Simulation of the Joint Dynamics

Initial simulations of a 3 DOF joint actuated by 4 tendons were conducted to estimate a few features of the joint: the stability of the ball in the socket, the stiffness of the joint under open-loop control, the workspace available, and the sensitivity of the joint to tendon origin and insertion locations.

The system was modeled using Simulink, where the "controller" received the target angles for the joint and used the kinematics from (1) and (2) to find the target proximal displacements for the tendons. The current state of the ball joint was then determined using (7), below:

$$\ddot{\boldsymbol{\theta}} = \big(\mathbf{u} - \mathbf{B}\dot{\boldsymbol{\theta}} + \mathbf{P}(\boldsymbol{\theta})\mathbf{K}\ (\mathbf{h} + \mathbf{l})\big)/\mathbf{Jm}(\boldsymbol{\theta}), \tag{7}$$

where $\boldsymbol{\theta}$ represents the fixed-frame rotation angles of the joint. The tendons are assumed to act with a linear elasticity matrix $\mathbf{K}$, which may be a function of $\mathbf{h}$ due to changes in tendon stiffness with length. The position of the ball is used (with (1) and (2)) to find the lengths of the tendons on the ball, $\mathbf{l}$, which, along with actuator position $\mathbf{h}$, generate tensions in the tendons. The tensions are then used with the matrix $\mathbf{P}$ from (4) to find the torques applied to the ball that, along with viscous damping $\mathbf{B}$ and external loads applied $\mathbf{u}$, will cause joint motion. The viscous damping effects in each direction of rotation were assumed to be decoupled from the others, making $\mathbf{B}$ a diagonal matrix. Here, $\mathbf{Jm}(\boldsymbol{\theta})$ is the inertial tensor of the joint, which is a function of the joint angles. In order to simplify the simulations, centripetal and centrifugal forces were ignored. This is a reasonable assumption for many applications, as the forces generated by these effects, at low speeds and accelerations, are negligible when compared to friction and tendon forces.

The reachable workspace was estimated by finding the portion of the mechanically available workspace that has force closure. In a tendon-driven joint, force closure is a necessary condition for stability in a given position [7]. It refers to the ability of a tendon network to reach a certain position with a sufficient number of tendons in tension that joint motion is constrained. If the tension is supplied solely by the tendons (not an external force), there must be one more tendon than the number of DOFs in the joint. For a position to be within the workspace of a tendon-driven joint, it must be a position with force closure and it must be reachable (with force closure) from the rest of the workspace.

For a given static position, with no other torques applied to the joint, the tensions in each tendon can be found if one tendon has a known, positive tension value t_e. The torque vector of this tendon can then be removed from the matrix $\mathbf{P}(\boldsymbol{\theta})$, resulting in a reduced matrix $\mathbf{P}_\mathrm{r}(\boldsymbol{\theta})$ that will be square. The removed column can be transposed to form a vector, $\mathbf{f}_\mathrm{e}$. The tensions in the remaining tendons will be defined as $\mathbf{t}_\mathrm{r}$, as expressed in (8):

$$\mathbf{t}_\mathrm{r} = -\mathbf{P}_\mathrm{r}(\boldsymbol{\theta})^{-1}(t_\mathrm{e}\mathbf{f}_\mathrm{e}). \tag{8}$$

If all of the resulting tensions are positive, the position has force closure and may be a stable position. The initial tests exploring the sensitivity of the joint to tendon layout were conducted simply by manually altering the tendon layout in this model and examining how changes influenced joint stability, stiffness, and workspace volume.

D. Open-Loop Control

An open-loop control strategy that increased the stiffness of the joint was tested in simulation. The strategy applied a minimum pretension $t_{\min}$ across the tendon network, rather than assuming that all tensions would be zero when the joint is stationary. In this approach, (8) becomes:

$$\mathbf{t}_\mathrm{r} = -\mathbf{P}_\mathrm{r}(\boldsymbol{\theta})^{-1}(t_{\min}\mathbf{f}_\mathrm{e}). \tag{9}$$

This equation is used in an iterative manner, starting with an arbitrary tendon to create $\mathbf{f}_\mathrm{e}$ and $\mathbf{P}_\mathrm{r}$ and which is assumed to act with the minimum tension, $t_{\min}$. From the generated tensions, the tendon with the smallest tension is then used to create a new $\mathbf{f}_\mathrm{e}$ and $\mathbf{P}_\mathrm{r}$, have $t_{\min}$ applied to it, and generate a new set of tendon tensions, $\mathbf{t}_\mathrm{r}$. The vector $\mathbf{t}_\mathrm{r}$ will be missing the tension value for the tendon with $t_{\min}$. This value can then be reinserted to form $\mathbf{t}$, in which the smallest tension will be $t_{\min}$. The vector of additional proximal tendon motion, $\mathbf{h}_\mathrm{t}$, that provides this tension can be found as:

$$\mathbf{h}_\mathrm{t} = \mathbf{K}^{-1}\mathbf{t}. \tag{10}$$

This motion, when added to the vector found from (2), will provide the $\mathbf{h}$ values that drive a sphere to a given position with the desired tension distribution, assuming no other forces act upon the joint. This is a variation of the method used in [8] to gain the optimal tension distribution for a manipulator with tendons passing through free space.

To compensate for tendon stretch caused by loads applied to the joint, (9) may be refined as follows:

$$\mathbf{t}_\mathrm{r} = \mathbf{P}_\mathrm{r}(\boldsymbol{\theta})^{-1}(K_\mathrm{g}\mathbf{P}(\boldsymbol{\theta})\mathbf{t}_\mathrm{ob} - t_{\min}\mathbf{f}_\mathrm{e}), \tag{11}$$

where $\mathbf{t}_\mathrm{ob}$ are the observed tensions and K_g is a gain factor. To ensure that the controlled system remains stable, K_g must be less than 1; otherwise, the controller will react to tensions introduced by inertial forces in an overly aggressive manner.

It is likely that a nonlinear control strategy such as that proposed in [9] would prove far more effective than the proportional control strategy outlined here. Additionally, as the distance between the actuators and the manipulator is made longer and tendon–sheath interactions become more influential, it may prove necessary to introduce specific compensation for this effect, as proposed in [10], [11].

E. Visual Servoing

A closed-loop control system for the joint was developed that utilizes visual servoing to reduce joint positioning error through a position-based dynamic look-and-move approach [12]. Based on the transformations between actuator and joint space, the visual servoing of this device can be handled as any other device controlled using a similar strategy.

Since the base of the joint and the end effector are both visually tracked, as seen in Fig. 3, and the target position is known relative to the base, this arrangement can be considered as a kind of end-point closed-loop visual servoing. This arrangement serves to nullify the influence of camera position, which significantly reduces the calibration required and makes the control system more robust.

For each observation of the joint end effector and base, an estimate of the joint rotation matrix, $\mathbf{R}_\mathrm{vis}$, was generated. By using this matrix as the rotation in (1) and (2), the proximal tendon motion, $\mathbf{h}_\mathrm{vis}$, can be estimated. This allows the error in joint position to be estimated as an error in the proximal tendon motion space (i.e., the difference between the vectors $\mathbf{h}_\mathrm{vis}$ and $\mathbf{h}$.). Thus, the control algorithm assumes that joint position error can be treated as an error in the proximal tendon displacement, feeding back a PI control signal to correct the error:

$$\mathbf{h}_\mathrm{t} = K_\mathrm{p\ vis}(\mathbf{h} - \mathbf{h}_\mathrm{vis}) + K_\mathrm{i\ vis}\int(\mathbf{h} - \mathbf{h}_\mathrm{vis})dt, \tag{12}$$

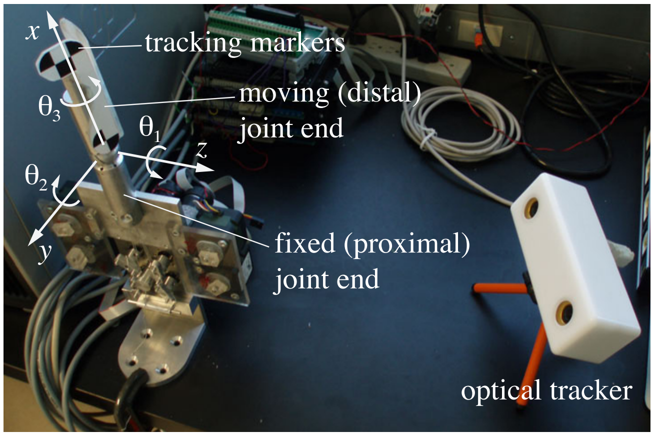

Fig. 3. Experimental joint apparatus with optical tracking system.

where $\mathbf{h}_{\mathrm{vis}}$ is the tendon displacement estimated using visual feedback. The variables $K_{\mathrm{p\ vis}}$ and $K_{\mathrm{i\ vis}}$ are the proportional and integral gains, respectively. This constitutes the control law of the outer loop within the look-and-move algorithm as described in [13].

Through experimental testing of this controller it was observed that tension would be lost in a tendon if an origin and insertion were much closer together than intended, leading to a build up of slack and in some cases instability. Such a situation could arise when slack is fed to the lower tensioned tendon faster than it can be taken in from the opposing higher tension tendons. This led to two modifications to the control law (12). The first change limits potential slack by limiting the magnitude of the $\int(\mathbf{h}-\mathbf{h}_{\mathrm{vis}})dt$ by a saturation value. The second change schedules the $K_{\mathrm{i\ vis}}$ gain so that it changes depending on the sign of $\int(\mathbf{h}-\mathbf{h}_{\mathrm{vis}})dt$. This change allows a given error integral to result in more actuator motion when increased tension is required than if increased slack is required. These two modifications were observed to help maintain tension within the tendon network.

F. *Experimental Testing*

Initial physical testing of this system was conducted with the prototype shown in Fig. 3. The joint was turned from 25 mm 6061 aluminum round stock. The tendons were made from 0.45 mm Dyneema/Nylon (Berkley 50 lb test Gorilla Braid). These tendons where driven using a set of motors: Maxon 305007 paired with 1024 pulse/rev quadrature encoders driven by Maxon ADS 50/10 servo amplifiers. This setup was controlled using a Sensoray model 626 multifunction I/O board coupled with a PC, along with feedback from the optical tracking system, in a fixed camera arrangement shown in Fig. 3. The servo motors were driven by an inner control loop using PID control through the I/O board with a proportional gain of 33.5 A/rad, an integral gain of 3.35 A/(rad·s), and a differential gain of 0.034 A·s/rad.

The outer loop control system used with the actual joint was an open-loop strategy with no control over system pretension, using (1) and (2) alone as the controller. Thus, without joint position feedback to compensate for errors, the accuracy results are representative of the accuracy of the joint kinematics presented herein, rather than the efficacy of a control algorithm in compensating for model inadequacies.

Joint position was measured using a MicronTracker optical tracking system, from Claron Technology Inc. This system provides 6 DOF tracking with a maximum position error ±0.25 mm, or approximately ±0.24° for θ_1 and θ_2 and ±1° for θ_3 rotation. The tracking system was used with a tracked stylus to register the axes of rotation for the joint. By constructing a least squares fit of the measured surface of the joint ball to a sphere, the origin could be located at its center. A similar procedure was preformed to find the x-axis, which passes along the central axis of the cylinder forming the base of the joint. A third registration was used to find the x-y plane passing through one of the tendon origins. This procedure allowed the motion reported by the tracking system to be translated into rotations as perceived by the controller, so that tracking error could be assessed. This same tracking system was also used to provide feedback for visual servoing.

III. RESULTS AND DISCUSSION

Results from testing the prototype joint are shown in Fig. 4. These results show that the joint performs as expected under open-loop control with no pretension. The driven angle tracks its reference with less than 5° error with a visible phase lag. The trajectory also consistently undershoots the peak reference values, likely due to the effects of friction within the joint. It appears that effects not being compensated for by the open-loop control system (e.g., gravity, tendon/apparatus compliance, or tendons shifting within their origins [4]) caused motion around the other axes of approximately 4°.

Some of the error apparent in Fig. 4 may also be due to inaccurate measurements of the origin and insertion locations [4]. During the development of the prototype it was observed that controller accuracy was sensitive to any errors introduced in these values. Errors in the supposed origin or insertion location of about 1 mm could dramatically affect the trajectory of the joint, on the order of 20°, as the tendon in question could not be moved appropriately. Additionally, some of this error is likely due to the fact that the tendon tensions were not initialized in a manner that made them known to the controller. At startup, the tension distribution may have been such that joint friction was preventing motion while the tendon tensions where not in equilibrium. Such a situation would be equivalent to starting the joint in a position slightly different than that assumed by the controller. This initial error would cause the actual relationship between joint and tendon motion to be slightly different than that calculated by the controller, causing errors in the trajectory.

Significant, high frequency motion of the joint around the θ_3 axis can be seen in the measurements of link motion reported. In practice, such motion was not physically observed. These oscillations are an artifact of the tracking system set up, which from Fig. 3 can be seen to have very short distances between tracking targets and the x-axis. This arrangement has rendered the tracking system less sensitive to motion around this axis and resulted in significant random error in the measurement of θ_3 . Motion in the θ_3 direction results in less motion of the actual tracker targets than motion around θ_1 or θ_2. With the furthest tracking target being about 19 mm away from the x-axis and the tracking system accuracy being 0.25 mm, we would expect errors on the order of $\pm 1^\circ$. This estimate conforms well to the error magnitudes actually seen in the θ_3 measurements.

A. Validation of Simulations

By comparing the results of the experimental tests to those garnered from simulation of the constructed joint, errors in the dynamic model should be made readily apparent by discrepancies with the actual link behavior. Such a comparison can be seen in Fig. 4 and Fig. 5. In this example the joint geometry used in simulation was that measured from the actual constructed joint, excluding the fact that the origin and insertion holes are significantly larger than the tendons. One further simplification made here was that the dynamics of the motors were entirely ignored. Instead, the measured motor positions from experimentation were used to drive the simulation. Removing the motor dynamics from the simulation reduced uncertainty in the model, allowing a more accurate evaluation of the joint model to be performed.

From the results in Fig. 4 we can see that the model used in simulation is representative of the actual behavior of the joint. Of particular importance is the fact that the motion of θ_2 and θ_3, when θ_1 is being driven, matches well. This result indicates that the tracking errors of θ_2 and θ_3 are not predominantly due to a poor estimate of the origin locations in the control algorithm, a misrepresentation of the joint kinematics, the effects of tendon thickness, or deviation from a circular tendon path due to constructed joint geometry. Since these influences were not included in the model, these sources of error would not have been captured in simulation. With these sources eliminated, the tracking errors likely stemmed from the effects of friction, tendon stretch, and gravity.

The simulated driven angle θ_1 consistently reached a higher peak value than actually occurred. This discrepancy was likely due to stiction of the joint near the apex of its motion due to dry friction. This mechanism was not captured by the simulation, which represented friction as purely viscous. Dry friction would be expected to cause a brief period of stiction which would start as soon as tendon motion reversed direction (the reference peak). At this time the torques generated by the tendons would become less than those required to overcome friction and motion would stop. Examination of Fig. 4 reveals this to be what occurs. The plateau lasts until tension has built in the tendons pulling in the new direction, leaving the joint with an element of apparent backlash similar to that reported in [14]. Attempts were made to include dry friction in the simulated model; however, these proved too computationally expensive to be practical. The conformance of the simulation with experimental results, for θ_2 being driven, proved virtually identical to those reported for θ_1.

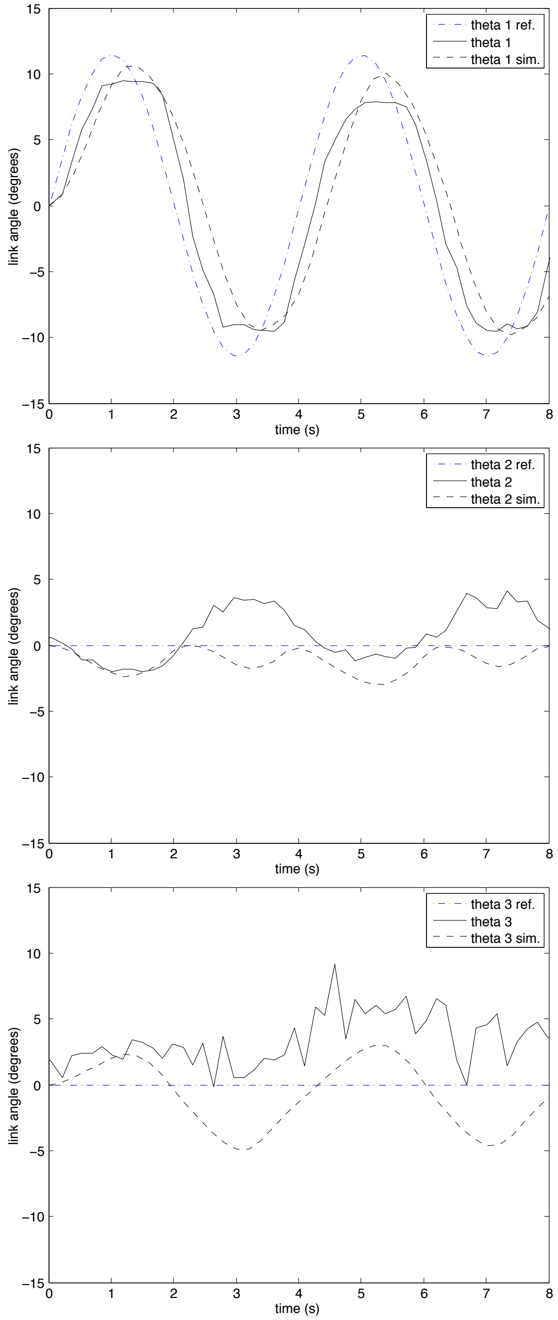

Fig. 4. Driving θ_1 through a sine wave using open-loop control. Both simulated results and optically-tracked observations are presented.

Similar results were observed when θ_3 was driven, as shown in Fig. 5, with the simulated and experimental joint motion matching quite well. In these results, the peak tracking error in θ_3 is consistently overestimated in simulation by about 3°. However, the results from the simulations are clearly representative of those observed with θ_1 and θ_2 matching within at least 5°. The simulated model appears to represent the behavior of the actual mechanical joint well and may be used in the development of new joints and control strategies.

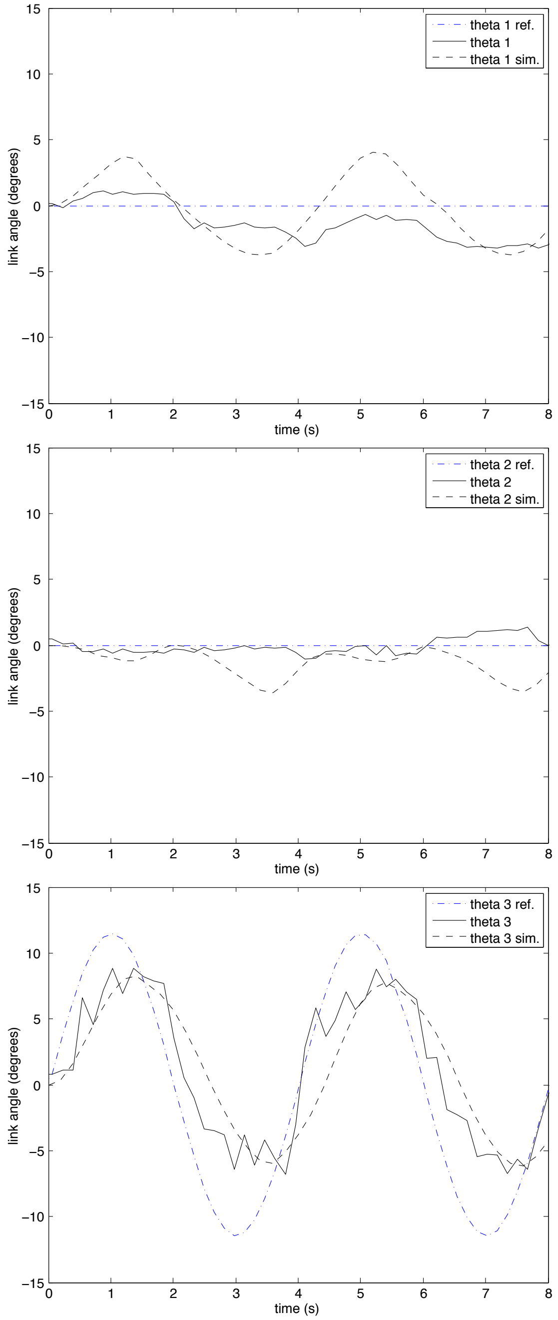

Fig. 5. Driving θ_3 through a sine wave using open-loop control. Both simulated results and optically-tracked observations are presented.

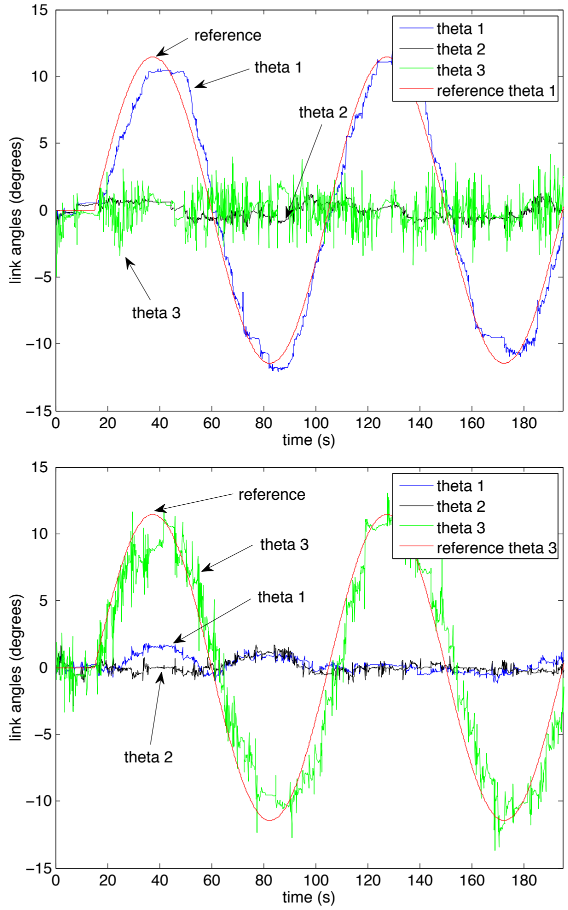

Fig. 6. Joint angles as recorded by optical tracking while driving angles θ_1 and θ_3 through a sine wave using visual servoing.

B. Visual Servoing of the Joint

Visual servoing can clearly be seen as a valid means of reducing joint positioning error as shown in Fig. 6. From these tests, we can see that the reference angle can be tracked with greater accuracy than was possible with the open-loop system. This is particularly visible in the angles with zero reference where the maximum error has been halved.

An error not found in the previous tests is visible in the results obtained under visual servoing. The error in the driven angle remains quite high, about 2°, for the first half cycle of motion. This temporary error likely occurred due to inappropriate initial tensions in the tendons that were gradually absorbed by the integrator term of the visual servo control law. This initial error is smaller than the peak error values observed under open-loop control. It was observed that the time needed to absorb this error was reduced by using larger controller gains in (12). However, increased $K_{\mathrm{i\ vis}}$ was seen to result in instability under certain conditions. Closed loop tension control could reduce this source of error, although it would increase the complexity of the control task.

In testing, $K_{\mathrm{p\ vis}}$ = 0.95, while $K_{\mathrm{i\ vis}}$ = 0.131/s and $K_{\mathrm{i\ vis}}$ = 1.01/s were used with negative and positive $\int(\mathbf{h}-\mathbf{h}_{\mathrm{vis}})dt$ respectively, in order to help maintain tension throughout the tendon network. The integrator $\int(\mathbf{h}-\mathbf{h}_{\mathrm{vis}})dt$ was set to saturate at a minimum value of -0.25 mm/s to limit the amount of slack that could accumulate in the tendon network due to the integrated visual error. The controller gains were selected through a manual tuning process and, though effective, may not be optimal.

Without the saturation feature, substantial slack was seen to accumulate on the side of the joint the link was leaning toward, since the motors could move more readily on the slack side than the tensioned side. This slack would then allow the link to flop past vertical and overshoot its target, leading to significant tracking errors and instability.

IV. CONCLUSION

The joint presented here simplifies the mechanical design of a tendon driven spherical joint by incorporating all three degrees of freedom into a single joint. This serves to eliminate any instances in which a set of tendons must be routed through a joint: a significant simplification when compared to previously designed 3 DOF wrists [15]. By using a true spherical joint, the singularities inherent in a spherical wrist consisting of orthogonal rotary joints are eliminated. Herein, it has clearly been demonstrated that such a joint can be driven through a range of motion suitable for many applications.

The parallel nature of this joint does complicate the control task when compared to simpler, serial joint designs. To achieve predictable, controlled motion of the joint, the motion of all actuators must be closely coordinated due to the fact that the joint and tendons comprise a redundant, parallel mechanism. However, this parallelism also serves to allow load sharing between actuators, decreasing actuator power requirements compared to serial joint arrangements.

Using visual servoing, the joint can be controlled precisely. The major disadvantage of this approach is the stereoscopic vision system that such an arrangement requires. In applications that are not suitable for optical tracking, alternative methods, such as electromagnetic tracking, may be substituted.

The joint proposed in this work is mechanically simple, having a minimal number of moving parts generating three degrees of freedom. Being so simple, such a design could easily be miniaturized. This joint provides an ideal candidate for use in micro-manipulators and many emerging robotics applications where size is critical.

ACKNOWLEDGMENT

The authors are grateful to Rajni V. Patel for his support and participation in useful discussions related to this work.

REFERENCES

[1] H. Wang, W. Chen, Y. Lei, and S. Yu, "Kinematic analysis and simulation of a 7-DOF cable-driven manipulator," in *IEEE International Conference on Control and Automation*, Rome, Italy, Apr. 10–14, 2007, pp. 642–647.

[2] K. Koganezawa and M. Yamazaki, "Mechanical stiffness control of tendon-driven joints," in *IEEE/RSJ International Conference on Intelligent Robots and Systems*, vol. 2, Kyongju, Korea, Oct. 17–21, 1999, pp. 818–825.

[3] S. Mustafa, G. Yang, S. H. Yeo, W. Lin, and C. B. Pham, "Development of a bio-inspired wrist prosthesis," in *IEEE Conference on Robotics, Automation, and Mechatronics*, Bangkok, Thailand, June 7–9, 2006, pp. 1–6.

[4] G. Cannata and M. Maggiali, "Models for the design of bioinspired robot eyes," *IEEE Transactions on Robotics*, vol. 24, no. 1, pp. 27–44, 2008.

[5] M. Hiller, S. Fang, S. Mielczarek, R. Verhoeven, and D. Franitza, "Design, analysis and realization of tendon-based parallel manipulators," *Mechanism and Machine Theory*, vol. 40, pp. 429–445, 2005.

[6] R. M. Murray, Z. Li, and S. S. Sastry, *A Mathematical Introduction to Robotic Manipulation*. New York, NY: CRC Press, 1994.

[7] C. B. Pham, S. H. Yeo, G. Yang, M. S. Kurbanhusen, and I.-M. Chen, "Force-closure workspace analysis of cable-driven parallel mechanisms," *Mechanism and Machine Theory*, vol. 41, pp. 53–69, 2006.

[8] F. Shiqing, D. Franitza, M. Torlo, F. Bekes, and M. Hiller, "Motion control of a tendon-based parallel manipulator using optimal tension distribution," *IEEE Transactions on Mechatronics*, vol. 9, pp. 561–568, 2004.

[9] H. Kobayashi and R. Ozawa, "Adaptive neural network control of tendon-driven mechanisms with elastic tendons," *Automatica*, vol. 39, pp. 1509–1519, Sept. 2003.

[10] M. Kaneko, W. Paetsch, and H. Tolle, "Input-dependent stability of joint torque control of tendon-driven robot hands," *IEEE Transactions on Industrial Electronics*, vol. 39, pp. 96–104, 1992.

[11] M. Kaneko, T. Yamashita, and K. Tanie, "Basic considerations on transmission characteristics for tendon drive robots," in *IEEE International Conference on Advanced Robotics*, vol. 1, Pisa, Italy, June 19–22, 1991, pp. 827–832.

[12] G. Taylor and L. Kleeman, *Visual Perception and Robotic Manipulation: 3D Object Recognition, Tracking and Hand-Eye Coordination*, ser. Springer Tracts in Advanced Robotics, B. Siciliano, O. Khatib, and F. Groen, Eds. Springer, 2006, vol. 26.

[13] S. Hutchinson, G. Hager, and P. Corke, "A tutorial on visual servo control," *IEEE Transactions on Robotics and Automation*, vol. 12, no. 5, pp. 651–670, Oct. 1996.

[14] G. Palli and C. Melchiorri, "Model and control of tendon-sheath transmission systems," in *Proc. IEEE Int. Conf. on Robotics and Automation*, Orlando, Florida, May 15–19, 2006, pp. 988–993.

[15] M. E. Rosheim, *Robot Wrist Actuators*. Wiley, 1989.

APPENDIX I

Under tension, the tendons will shift to the shortest available path between their origin and insertion points, minimizing the potential energy that they store. If the origin and insertion are points on the surface of the sphere, the path taken will be a circular arc concentric to the sphere, neglecting the dynamics of the tendon moving on the sphere surface. The angle subtended by this arc will be defined by lines formed between the sphere center and the origin and insertion points:

$$\arccos\left(\frac{\mathbf{R}\,\mathbf{I}_n}{r}\cdot\frac{\mathbf{O}_n}{r}\right). \tag{13}$$

With the angle measured in radians, the length of the arc will be defined as:

$$L_n = r\arccos\left(\frac{\mathbf{R}\,\mathbf{I}_n}{r}\cdot\frac{\mathbf{O}_n}{r}\right). \tag{14}$$

APPENDIX II

Given the proof outlined in Appendix I, and the assumptions made there, any tensioned tendon will pass along a plane defined by its origin, insertion, and sphere center. The tendon will only be able to exert a torque on the sphere around a vector perpendicular to this plane, in the direction:

$$\mathbf{R}\,\mathbf{I}_n \times \mathbf{O}_n. \tag{15}$$

The magnitude of this torque will be the product of the radius of the sphere and the tension in the tendon. Combining this with the direction vector, the exerted torque may be expressed as:

$$\boldsymbol{\tau}_n = t_n \quad (\mathbf{R}\,\mathbf{I}_n \times \mathbf{O}_n)/r. \tag{16}$$